Carbon 129 (2018) 527–536

Contents lists available at ScienceDirect

Carbon

journal homepage: www.elsevier.com/locate/carbon

High-yield single-step catalytic growth of graphene nanostripes by plasma enhanced chemical vapor deposition

Chen-Chih Hsu [a], Jacob D. Bagley [b], Marcus L. Teague [a], Wei-Shiuan Tseng [a, c], Kathleen L. Yang [a], Yiran Zhang [a], Yiliang Li [a], Yilun Li [d], James M. Tour [d], N.-C. Yeh [a, e, *]

[a] Department of Physics, California Institute of Technology, Pasadena, CA 91125, United States
[b] Department of Chemistry, California Institute of Technology, Pasadena, CA 91125, United States
[c] Graduate Institute of Photonics and Optoelectronics and Department of Electrical Engineering, National Taiwan University, Taipei 106, Taiwan
[d] Department of Chemistry, Department of Materials Science and NanoEngineering, The Smalley-Curl Institute and NanoCarbon Center, Rice University, Houston, TX 77005, United States
[e] Kavli Nanoscience Institute, California Institute of Technology, Pasadena, CA 91125, United States

ARTICLE INFO

Article history:
Received 1 November 2017
Received in revised form
14 December 2017
Accepted 15 December 2017
Available online 16 December 2017

ABSTRACT

We report a single-step growth process of graphene nanostripes (GNSPs) by adding certain substituted aromatics (*e.g.*, 1,2-dichlorobenzene) as precursors during the plasma enhanced chemical vapor deposition (PECVD). Without any active heating and by using low plasma power ($\leq$60 W), we are able to grow GNSPs vertically with high yields up to (13 ± 4) g/m^2 in 20 min. These GNSPs exhibit high aspect ratios (from 10:1 to >~130:1) and typical widths from tens to hundreds of nanometers on various transition-metal substrates. The morphology, electronic properties and yields of the GNSPs can be controlled by the growth parameters (*e.g.*, the species of seeding molecules, compositions and flow rates of the gases introduced into the plasma, plasma power, and the growth time). Studies of the Raman spectra, scanning electron microscopy images, ultraviolet photoelectron spectroscopy, transmission electron microscopy images, energy-dispersive x-ray spectroscopy and electrical conductivity of these GNSPs as functions of the growth parameters confirm high-quality GNSPs with electrical mobility ~10^4 cm^2/V-s. These results together with residual gas analyzer spectra and optical emission spectroscopy taken during PECVD growth suggest the important roles of both substituted aromatics and hydrogen plasma in the rapid vertical growth of GNSPs with large aspect ratios.

1. Introduction

Among many intriguing properties and promising applications of graphene-based materials [1–3], reduced dimensional graphene nanostructures, such as graphene nanoribbons (GNRs) that often refer to one-dimensional crystals with nanoscale widths, have attracted much attention for their quantum confinement effects in extremely narrow ribbons [4,5], novel edge characteristics [3,6–8], mechanical strength [9,10], and a wide range of technological prospects in such areas as nano-electronics [11–15], spintronics [16,17], plasmonics [18–20], biosensors [21,22], energy storage [23], and energy production [24].

One of the primary challenges to fully realize the technological promises of reduced dimensional graphene nanostructures is to reliably produce a large quantity of high-quality nanomaterials with large aspect ratios. In general, the structural and physical properties of reduced dimensional graphene nanostructures are strongly depending on the synthesis method. To date, the best known methods for synthesizing quasi-one dimensional graphene nanostructures include the following primary categories: [1] The top-down approach, which utilizes lithographic techniques to produce GNRs from two-dimensional graphene sheets on a substrate. The quantities of GNRs thus produced are limited due to the time consuming lithographic processes, and the edges of these GNRs are usually jagged [25,26]. [2] The bottom-up approach, which may be further divided into the surface-assisted [27,28] and solution-phase synthesized [29–35] approaches. The surface assisted method involves pre-synthesis of polymer chains on metallic substrates and has the advantage of achieving atomically

* Corresponding author. Department of Physics, California Institute of Technology, Pasadena, CA 91125, United States.
E-mail address: ncyeh@caltech.edu (N.-C. Yeh).

https://doi.org/10.1016/j.carbon.2017.12.058

precise armchair- or zigzag-edges [7,8,27,28]. However, this approach generally involves multiple steps of processing, which leads to very low yields and relatively short GNRs. Moreover, these GNRs are not easily transferrable to other substrates. Similarly, the solution-phase synthesized approach also involves multiple steps and the resulting GNRs exhibit a range of controlled widths on the order of 1–2 nm and typical lengths over 100 nm [29–35]. While both types of bottom-up approaches can achieve better control of the structures of GNRs, the complexity in the synthesis procedures and the relatively low yields are not ideal for mass production in large-scale applications. [3] Unzipping carbon nanotubes (CNTs): Multi-walled CNTs can be unzipped along the longitudinal direction to form GNRs [36,37]. Compared to the first two methods, this approach has the potential of mass production and lower costs. However, the process is time consuming and also requires initial mass production of CNTs. The GNRs thus produced also contain excess metallic impurities [38,39]. [4] Growth by thermally assisted plasma enhanced chemical vapor deposition (PECVD): Synthesis of vertically oriented graphene "nanowalls" or "nanosheets" by means of PECVD have been reported for a variety of precursor gases [40,41]. However, this method faces three major challenges [40]: First, all processes reported to date involve multiple steps of pretreatment of the substrates as well as high-temperature (ranging from 500 °C to 1150 °C) substrate heating and high plasma power ($>10^2$ W and up to ~ 10^3 W) during the graphene growth [40,41]. Second, the yields are generally too low to be practical for mass production [40,41]. Third, the morphology and structures of vertically grown graphene nanosheets are not well controlled [40,41] because the growth mechanisms under different growth parameters and precursor molecules are not fully understood.

To overcome the aforementioned challenges, we report in this work a new single-step seeded growth method of "graphene nanostripes" (GNSPs) by PECVD techniques that can achieve high-yield and high-quality growth of GNSPs reliably without any active heating. The lengths of these GNSPs range from a few to tens of micrometers and the widths range from tens to hundreds of nanometers. Therefore, they exhibit large aspect ratios (typically from 10:1 to >~130:1) but do not manifest effects of quantum confinement. Further, their widths are typically narrower than most nanowalls and nanosheets reported to date [40,41]. Therefore, we refer these quasi-one dimensional nanostructures to "graphene nanostripes" (GNSPs) to indicate their large aspect ratios and to differentiate them from GNRs that exhibit quantum confinement and also from graphene nanosheets [40] or nanowalls [41] that are generally wider and are with smaller aspect ratios than our GNSPs.

In comparison with our single-step PECVD growth process of high-quality large graphene sheets *laterally* on copper substrates without active heating [42], these GNSPs of large aspect ratios are grown *vertically* on various transition-metal substrates by PECVD with the addition of substituted aromatics such as 1,2-dichlorobenzene (1,2-DCB), 1,2-dibromobenzene (1,2-DBB), 1,8-dibromonaphthalene (1,8-DBN) and toluene as the seeding molecules. Among these substituted aromatics, we find that 1,2-dichlorobenzene (1,2-DCB) is most effective for the growth of GNSPs at room temperature, as detailed in the supplementary information. Therefore, we focus hereafter on the studies of PECVD-grown GNSPs that are seeded by 1,2-DCB.

The entire growth process occurs in a single step within less than 20 min at a relatively low plasma power (≤60 W), and the resulting GNSPs exhibit large aspect ratios and high yields. Studies of the Raman spectroscopy, scanning electron microscopy (SEM), transmission electron microscopy (TEM), energy dispersion x-ray spectroscopy (EDS), ultraviolet photoemission spectroscopy (UPS) and electrical conductivity all confirm the high quality of the GNSPs thus obtained. Based on these experimental findings together with data from the residual gas analyzer (RGA) spectra and optical emission spectroscopy (OES) taken during the plasma process, we propose a growth mechanism and suggest that the introduction of substituted aromatics in the hydrogen plasma plays a critical role in achieving rapid vertical growth of GNSPs with high aspect ratios.

2. Experimental

2.1. Experimental setup

The PECVD system is schematically illustrated in Fig. S1. It consists an Evenson cavity and a power supply (MPG-4, Opthos Instruments Inc.) to generate plasma. The 1,2-DCB precursor is stored in a quartz container and attached to the growth chamber via a leak valve and a quarter-turn, shut-off valve. A residual gas analyzer (RGA) is used to monitor the precursor and by-products partial pressure.

2.2. Seeded growth of GNSPs

The quartz tube was pumped down to 27 mTorr. During the growth, the total pressure of the tube was maintained at 500 mTorr with 2 sccm hydrogen. The additional methane and 1,2-DCB was controlled by a precision leak valve and the partial pressure was monitored by a RGA. Typical methane and 1,2-DCB partial pressures were $(10–900) \times 10^{-9}$ Torr and $(1–10) \times 10^{-9}$ Torr, respectively, as measured in the RGA. Hydrogen plasma was formed away the substrate and then moved to the substrate in order to prevent any plasma transient damages. Typical plasma power ranged from 40 to 60 W with a plasma size of 1–2 cm^3, and growth time ranged from 0.5 to 20 min.

2.3. Characterization

The PECVD-grown GNSPs were characterized by Raman spectroscopy, UPS, XPS, SEM, TEM and electrical conductivity studies. Raman spectra were taken via a Renishaw M1000 micro-Raman spectrometer system using a 514.3 nm laser (2.41 eV) as the excitation laser source. The laser spot size was ~1 μm in diameter and the exposure time was 30 s. A 50 × objective lens with a numerical aperture of 0.75 and a 2400 lines/mm grating were chosen during the measurement to achieve better signal-to-noise ratio. The UPS were performed via the Kratos-Ultra-XPS model which uses a magnetic immersion lens with a spherical mirror and concentric hemispherical analyzers with a delay-line detector for both imaging and spectroscopy. He I (21.2 eV) were used as excitation sources for UPS measurement in an ultrahigh vacuum chamber with a base pressure of 2×10^{-10} Torr. The SEM images were taken by a FEI Nova 600 SEM system with the following parameters: acceleration voltage = 5 kV, beam current = 98 pA, and working distance ~5 mm. The TEM measurements were performed on a FEI Tecnai TF30 STEM (TF30) with an operating voltage of 300 KV. The electrical conductivity measurements were made by means of the four-probe method on GNSPs aligned on patterned electrodes via electrophoresis techniques.

3. Results and analyses

The seeded PECVD growth process is schematically illustrated in Fig. 1(a). We use 1,2-DCB to act as seeds for vertically aligned carpets of GNSPs grown on Cu surfaces. The hydrogen plasma with a slight trace of CN radicals is used to remove the surface copper oxide and expose fresh copper surface upon which 1,2-DCB molecules can seed [41], resulting in the initial formation of vertical GNSPs. Additionally, methane is introduced into the hydrogen

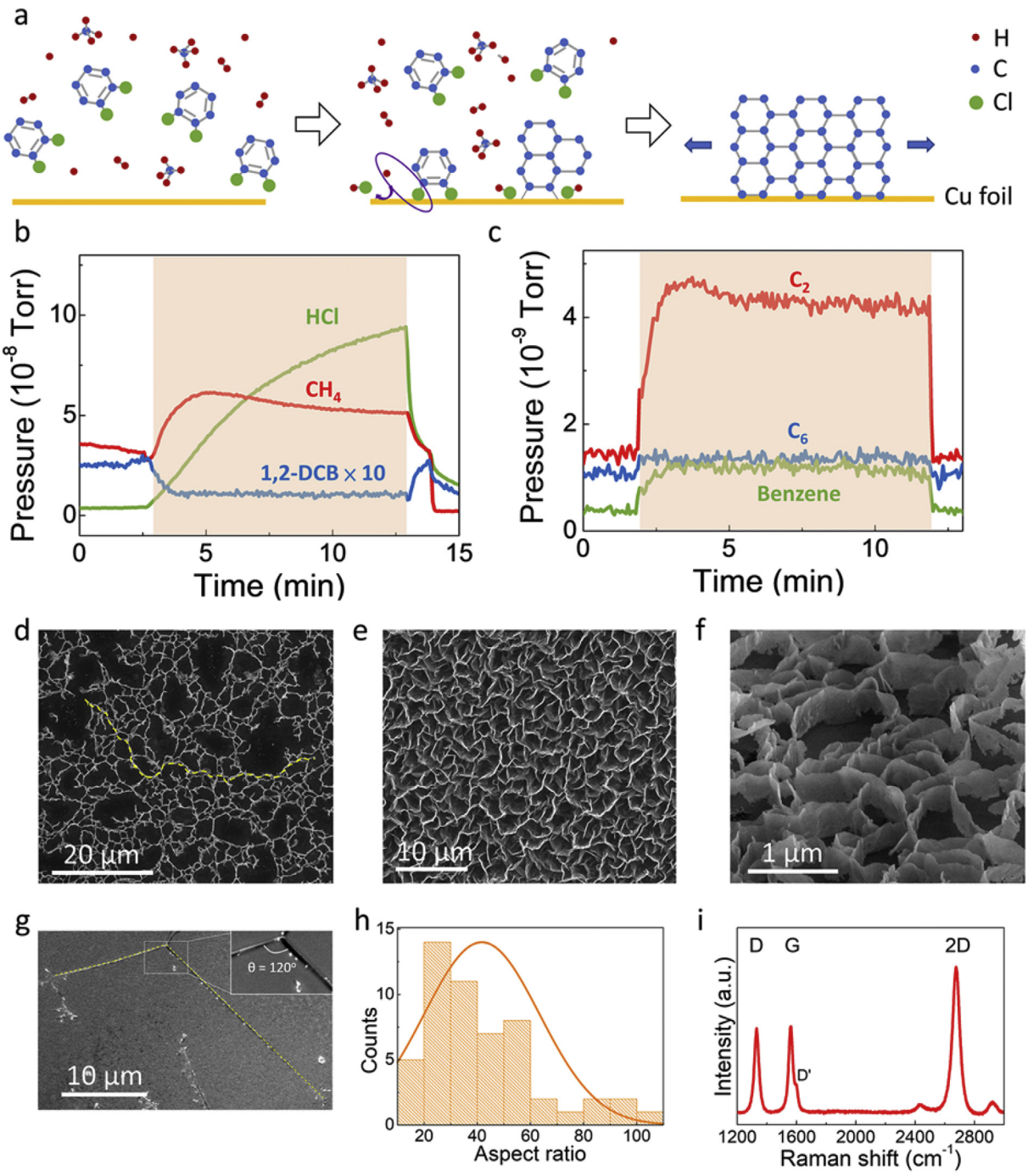

Fig. 1. **(a)** Schematic illustration of the seeded growth process of PECVD-grown GNSPs. **(b)**–**(c)** RGA spectra of gas pressures in the growth chamber as a function of time, where the shaded area indicated the duration of the plasma process. **(d)**–**(e)** Two representative SEM images of the top view of GNSPs on Cu foil fabricated by PECVD with 1,2-DCB molecules for 10 min **(f)** SEM image of the tilted view (at 52°) of GNSPs shown in (d), revealing a relatively constant width of ~500 nm for all GNSPs within the field of view. **(g)** SEM image of one GNSP isolated from the batch of GNSPs in (e) and placed on a silicon substrate, showing a length of ~66 μm (main panel) and a three-fold branching point near the end of the GNSP (inset). The GNSP in the main panel is highlighted by yellow dashed lines for clarity. **(h)** A representative histogram of the aspect ratios of GNSPs obtained from multiple sets of SEM images within their field of view. **(i)** A typical Raman spectrum of GNSPs. (A colour version of this figure can be viewed online.)

plasma as another carbon source to enhance the growth rate. We have also demonstrated the feasibility of using other carbon based, substituted aromatics such as 1,2-DBB, 1,8-DBN and toluene as precursors and different transition-metal substrates (such as Ni foam and Ni foil besides Cu foil), as exemplified in Figs. S2 and S3 for 1,2-DBB and 1,8-DBN, and in Fig. S4 for toluene.

The PECVD system is equipped with a residual gas analyzer (RGA) and an optical emission spectrometer (OES), which are used to monitor the gases in the growth chamber during the PECVD process. Two representative RGA spectra are shown in Fig. 1(b) and (c), where the shaded band indicates the time interval from turning on to turning off the plasma. The spectrum in Fig. 1(b) reveals that hydrogen chloride (HCl) is a main byproduct of the seeded PECVD growth process. This indicates that hydrogen radicals can react with chlorine in 1,2-DCB to form hydrogen chloride and render the resulting vertical GNSPS mostly free of chlorine. Additionally,

substantial amounts of C_2 and C_6 radicals together with C_6H_6 molecules are found during the plasma growth process, as shown in Fig. 1(c). We note that while C_2 are common radicals found in all previously reported thermally assisted PECVD growth [40], the eminent presence of C_6 radicals and C_6H_6 molecules are unique in our low-temperature PECVD process.

We have also monitored the optical emission spectra (OES) of the plasma during the growth process as a function of the 1,2-DCB/CH_4 partial pressure ratio, as shown in Fig. S5. We find that the intensities of all hydrogen related peaks (H_α, H_2 and H_β) decrease with increasing 1,2-DCB partial pressure, consistent with the reaction of hydrogen with increasing chlorine radicals. On the other hand, the intensity of C_2 radicals is enhanced upon the introduction of 1,2-DCB precursor molecules, although no further increase appears with increasing 1,2-DCB partial pressure.

Fig. 1(d) – (e) show two representative SEM images of the top view of GNSPs grown for 10 min with the growth parameters listed in the first row of Table 1, and Fig. 1(f) is the SEM image of a tilted view (at 52°) of the GNSPs shown in Fig. 1(d). These images together with the optical micrograph exemplified in Fig. S6(b) reveal that GNSPs uniformly distributed over the entire (1.2 cm × 0.8 cm) surface area of the Cu substrate. Moreover, we note that the widths of all GNSPs synthesized with a given set of PECVD growth parameters appeared to be nearly the same, as exemplified by the tilted view shown in Fig. 1(f) where the average width of GNSPs is ~500 nm. On the other hand, there is a range of length distributions for the GNSPs, and they are typically on the order of tens of micrometers, as exemplified by the yellow line in Fig. 1(d) from one open end to the other open end, and by the SEM image shown in Fig. 1(g) for an isolated GNSP that was transferred to a silicon substrate. Here we note that the real lengths of individual GNSPs are generally much longer than the distances between joint points revealed in the SEM images of as-grown GNSPs, as corroborated by Fig. 1(g).

To isolate and image individual GNSPs by SEM, we first immersed the copper substrate with as-grown GNSPs in dimethylformamide (DMF) solvent for ~ 9 h and then sonicated the solution for 3 min. A drop of the solution with dispersed GNSPs was placed on a silicon substrate and then heated at 175 °C until the solvent completely boiled off. GNSPs left on the silicon substrate were then imaged by SEM without further modification.

By analyzing the top views of multiple sets of SEM images for the length distributions of GNSPs and the tilted views for the average widths, we obtained a representative histogram for the aspect ratios of GNSPs in Fig. 1(h), showing a distribution from ~10 to >~130.

A representative Raman spectrum of the GNSPs is shown in Fig. 1(i), where three distinct peaks are visible [43–46]: The peak at ~2700 cm^{-1} is known as the 2D-band that represents a double-resonance process of graphene; the peak at ~1590 cm^{-1} is the G-band associated with the doubly degenerate zone-center E_{2g} mode of graphene, and the peak at ~1350 cm^{-1} is the D-band that corresponds to zone-boundary phonons due to defects, edges, and/or folds of graphene sheets [43–46]. Given that the laser spot of our Raman spectrometer (~1 μm) is larger than the typical widths (tens to hundreds of nanometers) of our GNSPs, we attribute the intense D-band of our GNSPs to the prevailing presence of edges and/or the presence of folds as observed in SEM and transmission electron microscopy (TEM) images. We further note that the 2D-to-G intensity ratio, (I_{2D}/I_G), is typically greater than 1 and that the full-width-half-maximum (FWHM) of the 2D-band is relatively sharp, which seems to suggest that our GNSPs are largely monolayer [43–47]. However, this notion contradicts the findings of multilayer GNSPs from our AFM and TEM studies. These seemingly inconsistent results can be reconciled by the presence of incommensurate rotation of one layer relative the adjacent layers of these multilayer GNSPs, as elaborated later in this manuscript. Moreover, the turbostratic multilayer structures of GNSPs may also be responsible for the appearance of a slight shoulder in the G-band peak, which is known as the D′-band that results from defects-induced intra-valley scattering [43,44].

To investigate the dependence of GNSPs growth on various parameters, we show in Fig. 2(a)–(c) SEM top view images of PECVD-grown GNSPs on Cu under different 1,2-DCB/CH_4 partial pressure ratios. The total gas pressure was 500 mTorr and the flow rate of H_2 was 2 sccm. With the CH_4 partial pressure kept constant at ~6×10^{-9} Torr during the growth, we found that the morphology of GNSPs was strongly dependent on the ratio of 1,2-DCB to CH_4 partial pressures. For instance, when the 1,2-DCB/CH_4 partial pressure ratio was ~1.5 or less, the resulting GNSPs grown on Cu had typical lengths of a few to tens of micrometers and relatively large aspect ratios, as exemplified in Fig. 2(a). With the partial pressure ratio of 1,2-DCB/CH_4 increased to ~1.8, the GNSPs began to branch out, as shown in Fig. 2(b). Upon further increase of the 1,2-DCB/CH_4 partial pressure ratio to ~2.4, a highly branched, flower-like nanostructure developed. These graphene "nano-flowers" (see Fig. 2(c)) were thinner and shorter than the typical GNSPs grown with a smaller 1,2-DCB/CH_4 partial pressure ratio. This trend was in part attributed to the high 1,2-DCB concentration that saturated the substrate and led to a high density of nucleation sites and therefore an overall decrease in the lateral size of GNSPs, as manifested in Fig. 2(c). The branching behavior in addition to the shorter lengths of the graphene nanostructures may be attributed to the large amount of 1,2-DCB that resulted in excess chlorine ions terminated along the edges of the GNSPs and activated the formation of the branching behavior. This scenario is consistent with studies of the ultraviolet photoelectron spectroscopy (UPS), TEM and energy-dispersive x-ray spectroscopy (EDS) of GNSPs as a function of the 1,2-DCB/CH_4 partial pressure ratio, to be elaborated below.

UPS experiments were conducted to investigate the work functions of GNSPs grown under different 1,2-DCB/CH_4 partial pressure ratios and to provide direct information about possible doping effects on GNSPs [48–50]. As shown in Fig. 2(d) and summarized in Fig. 2(g), the work function value (Φ) deduced from the secondary electron cutoff of the UPS spectrum was found to be

Table 1
Experimental parameters for the growth process, showing the gas partial pressures of 1,2-DCB and CH_4, plasma power, and time for the PECVD growth of GNSPs. The gas partial pressures were as measured in the RGA.

1,2-DCB (10^{-9} Torr)	CH_4 (10^{-9} Torr)	Power (W)	Growth time (min)	Yield (μg)
1–10	10–40	40	10	≤1
1–10	10–40	60	10	12 ± 6
1–10	900	60	5	350 ± 280
1–10	900	60	10	530 ± 130
1–10	900	60	15	800 ± 270
1–10	900	60	20	1300 ± 430

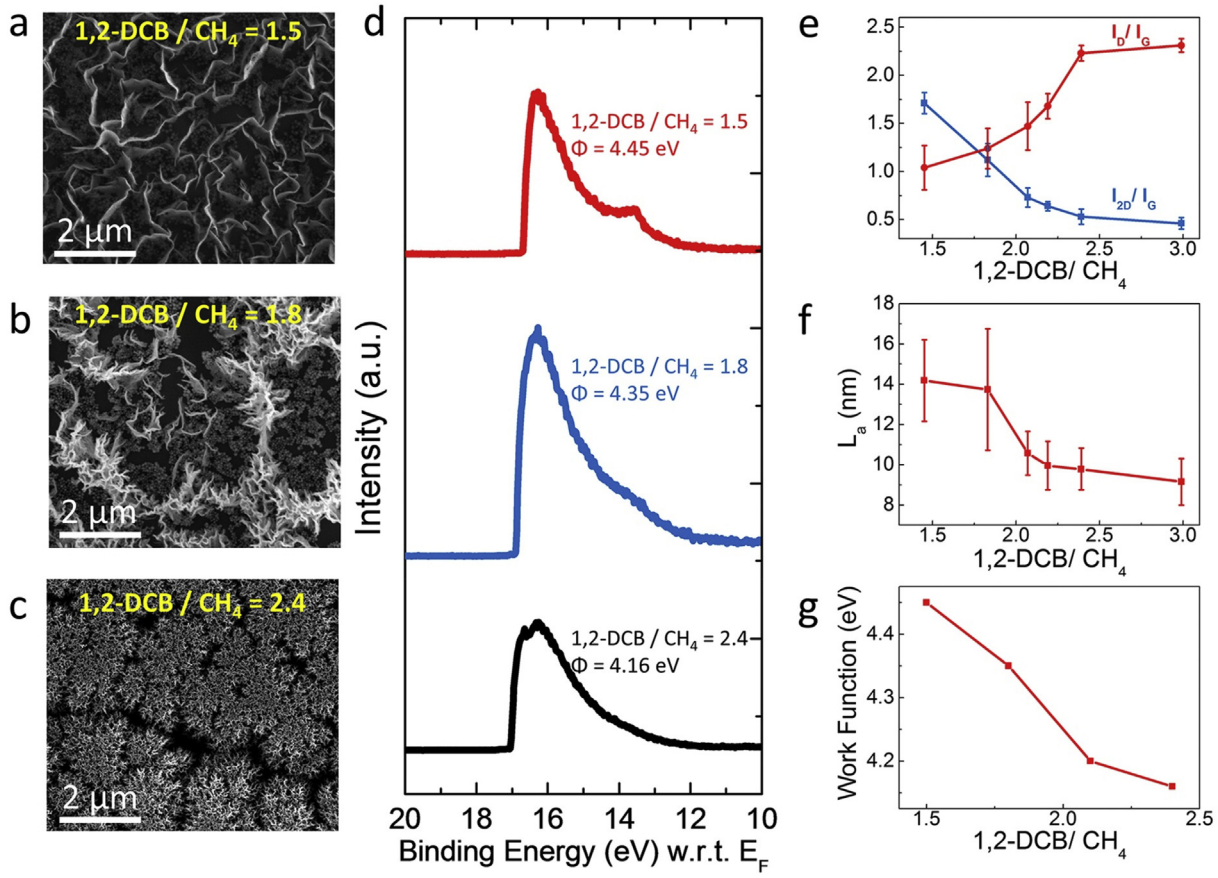

Fig. 2. Dependence of the surface morphology, work function, Raman spectroscopy and crystalline size of GNSPs on the 1,2-DCB/CH_4 partial pressure ratio: **(a)**–**(c)** SEM images of GNSPs with 1,2-DCB/CH_4 partial pressure ratio = 1.5 in (a), 1.8 in (b) and 2.4 in (c), showing increasing branching phenomena. **(d)** UPS data taken on GNSPs grown under 1,2-DCB/CH_4 partial pressure ratio = 1.5, 1.8 and 2.4, showing increasing electron doping. **(e)** Raman 2D/G and D/G intensity ratios of GNSPs grown under different 1,2-DCB/CH_4 partial pressure ratios. **(f)** Planar sp [2] crystallite size (L_a) and **(g)** work function of our GNSPs as a function of the 1,2-DCB/CH_4 partial pressure ratio. (A colour version of this figure can be viewed online.)

4.45 eV for GNSPs grown with a 1,2-DCB/CH_4 partial pressure ratio = 1.5, which is a value close to that of pristine graphene (~4.5 eV) [51]. The work function value decreased to 4.16 eV for GNSPs grown with a 1,2-DCB/CH_4 partial pressure ratio increased to 2.4, implying significant electron doping. This finding suggests that excess 1,2-DCB not only resulted in the formation of branches and excess chlorine in the GNSPs (see TEM and EDS results) but also introduced additional electron doping.

We further performed Raman spectroscopic studies on GNSPs grown under different 1,2-DCB/CH_4 partial pressure ratios. Fig. 2(e) shows the 2D to G intensity ratios, (I_{2D}/I_G), and D to G intensity ratios, (I_D/I_G), of GNSPs grown at different 1,2-DCB/CH_4 partial pressure ratios. The (I_{2D}/I_G) ratio decreases with the increase of 1,2-DCB/CH_4 partial pressure ratio, suggesting that more layers of GNSPs were grown [43,44] with larger amounts of 1,2-DCB. On the other hand, the (I_D/I_G) ratio increases with the increase of 1,2-DCB/CH_4 partial pressure ratio, which is consistent with more edges [43,44] due to branching. Additionally, the in-plane sp^2 crystallite size (L_a) of the GNSPS may be estimated by using the (I_D/I_G) ratio and the following empirical formula [52].

$$L_a(\mathrm{nm}) = \frac{560}{E_L^4}\left(\frac{I_D}{I_G}\right)^{-1}, \quad (1)$$

where E_L denotes the excitation energy of the laser source, which is 514 nm for our Raman spectrometer. We find that both the crystallite size L_a and the work function Φ of the GNSPs decrease steadily with increasing 1,2-DCB/CH_4 partial pressure ratio, as illustrated in Fig. 2(f) and (g), respectively.

In order to achieve high yields of GNSPs growth, we experimented various parameters for synthesizing typical GNSPs with 1,2-DCB/CH_4 partial pressure ratios <~1, as summarized in Table 1. We found that the yield of GNSPs, determined in units of mass per unit area, increased by more than one order of magnitude when the power was increased from 40 W to 60 W. This finding may be attributed to the presence of more energetic gas molecules and radicals (particularly C_2, C_6 and C_6H_6) in the plasma to initiate and maintain the growth of GNSPs. Additionally, higher CH_4 partial pressure and longer growth time provided more carbon sources and therefore also help increase the yield of GNSPs. On the other hand, further increase of either the plasma power above 60 W or the CH_4 partial pressure could not result in higher yields, which may be the result of a limited surface area of the Cu substrate in our growth chamber for initiating the vertical growth of GNSPs. Moreover, excess plasma power tends to increase the amount of C_2 radicals at the expense of reducing the amount of C_6 radicals and C_6H_6 molecules. Given that C_6 radicals and C_6H_6 molecules are likely playing an important role in enhancing the growth rate of GNSPs, proper balance between the plasma power and the amount of C_6 and C_6H_6 is necessary to achieve high yields of GNSPs.

By optimizing various growth parameters, we found that the best yield for 20 min of growth time could reach (1.30 ± 0.43) mg/

cm^2, or equivalently, (13.0 ± 4.3) g/m^2. The high-yield growth of GNSPs resulted in a completely darkened surface of the substrate due to dense coverage of GNSPs on the metallic substrate, as exemplified by the optical micrographs in Fig. S6 (a)-(b) and the nearly zero optical transmission from 400 nm to 800 nm shown in the main panel of Fig. S6. The completely darkened substrate surface by the coverage of GNSPs and the vanishing optical transmission is indicative of strong light absorption by GNSPs, which may be attributed to effective light trapping in stacks of GNSPs due to multiple scattering. Thus, GNSPs may be considered as efficient light absorbers for potential applications to photovoltaic cells when combined with proper plasmonic nanostructures [24].

Next, nanoscale structural properties and chemical compositions of the PECVD-grown GNSPs were investigated by means of TEM and EDS. Measurements were initially performed on standard GNSPs similar to those shown in Fig. 2(a). Fig. 3(a) ~ (c) are TEM top view images, with successively increasing resolution, of GNSPs grown with a 1,2-DCB/CH_4 partial pressure ratio ~ 1.5. From detailed TEM studies, we found that the typical size of GNSPs transferred to the TEM grid was 500 nm−1.0 μm in width and 5−10 μm in length, as exemplified in Fig. 3(a). The shorter lengths than those of the as-grown GNSPs (as represented by the histogram in Fig. 1(h)) may be attributed to the TEM sample preparation steps that involved sonication of GNSPs in solution that led to shortened samples.

These GNSPs were generally flat over large areas and exhibited ordered nanoscale structures, as illustrated in Fig. 3(b). High resolution images taken on these flat areas further revealed graphene atomic lattice structures, as shown in Fig. 3(c). We found that these GNSPs were mostly multilayers and turbostratic: From selected area diffraction (SAD) in Fig. 3(d), the sample exhibited two predominant orientations and exceeded 6 layers in thickness. This finding of multilayer GNSPs seems to differ from Raman

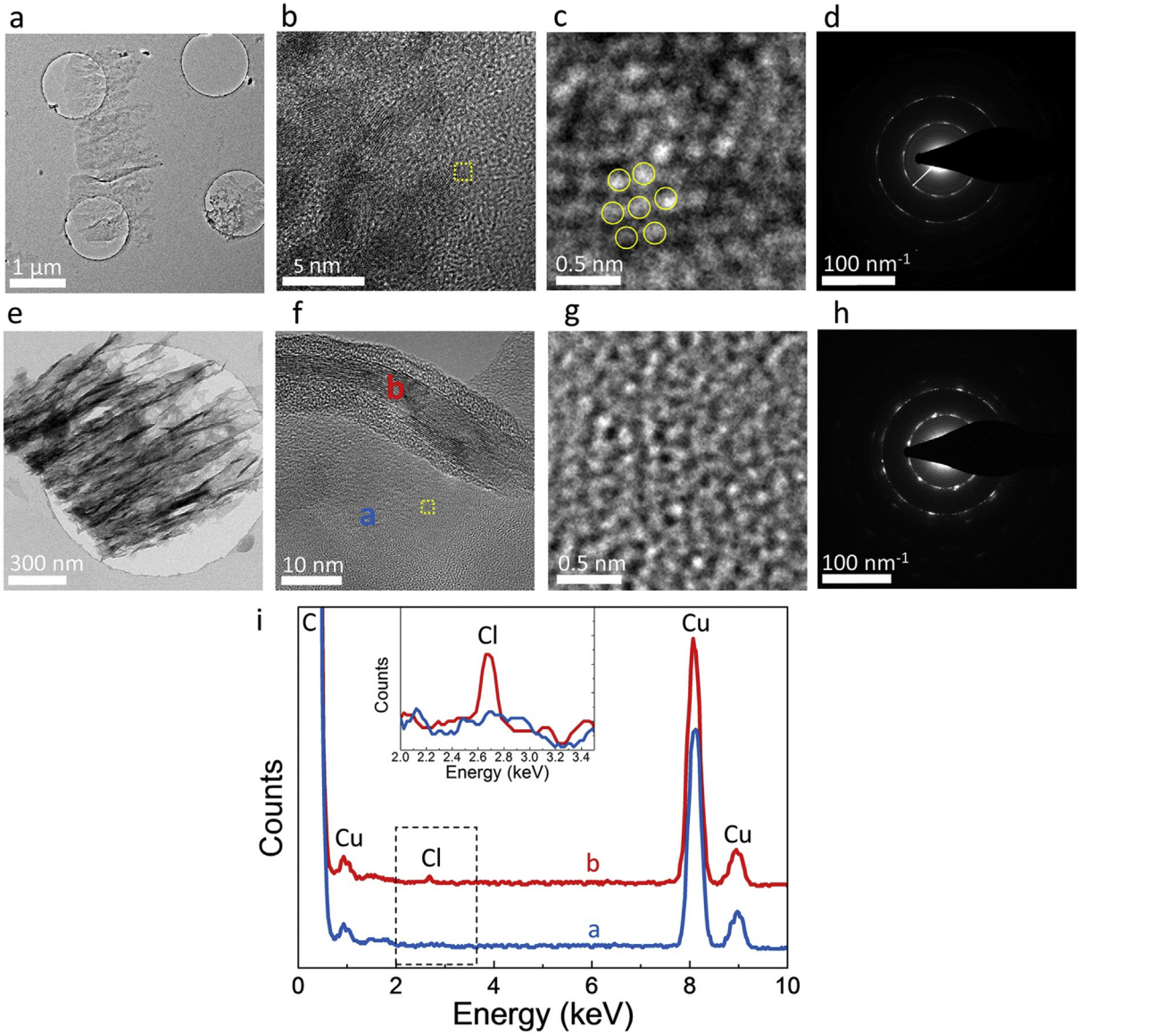

Fig. 3. (**a**)–(**c**) TEM top view images of GNSPs with successively increasing resolution from large scale to atomic scale images, with (c) being the expansion of a region indicated by the small yellow box in (b). **(d)** SAD pattern of GNSPs for the region shown in (c). **(e)**–**(f)** TEM top view images of graphene nanoflowers from large scale to atomic scale images, with (g) being the expansion of a region indicated by the small yellow box in (f). **(h)** SAD pattern of the sample region shown in (g). **(i)** EDS data shows a distinct chlorine peak on a branching region labeled by **b** in (f), which is in stark contrast to the absence of chlorine in flat areas such as the region labeled by **a**. The inset is an expansion of the dashed area shown in the main panel. (A colour version of this figure can be viewed online.)

spectroscopic studies of the same GNSPs that always revealed both (I_{2D}/I_G) ratios > 1 and relatively small FWHM in the 2D-band and so would seem to imply monolayer GNSPs [42,43,46]. However, we note that the Raman spectra of multilayer graphene sheets with turbostratic stacking (where individual layers separated by a larger than normal interlayer distance) were also found to exhibit (I_{2D}/I_G) ratios > 1 [53]. Therefore, our findings derived from the TEM studies of standard GNSPs can be reconciled with the Raman spectroscopic studies.

In addition to studies of the structural properties, we performed nanoscale EDS measurements on flat, unstrained regions of these standard GNSPs, and found a pure carbon composition without any chlorine or other contaminates. This finding is in contrast to studies of the "nano-flowers" samples where chlorine appeared in regions with bifurcations, branching or strain, as explained below.

In Fig. 3(e)-(g), we show TEM images with successively increasing resolution that were taken on nano-flower GNSPs grown with a 1,2-DCB/CH_4 partial pressure ratio ~ 2.3. In contrast to the typical images taken on standard GNSPs, Fig. 3(e) and (f) reveal that nano-flowers generally consisted of a large number of layers, with numerous branching points and reorientations of the layers. In particular, Fig. 3(f) shows that in the reoriented graphene region the number of graphene layers within the field of view is > 20, whereas graphene atomic structures can be resolved in flat regions, as exemplified in Fig. 3(g). Further SAD studies on a flat region of the sample in Fig. 3(f) exhibit a diffraction pattern that provides evidence for multiple layers, with varying orientations for many individual graphene layers that lead to the disordered circular pattern. On the other hand, a significant chlorine peak in the EDS data is always observed at a large number of branching and reorientation locations in the nano-flower samples, as exemplified in Fig. 3(i). This presence of a distinct chorine peak in a branching region of the nano-flowers is in stark contrast to the absence of any chlorine signal in the flat region of the same samples.

We also investigated the electrical properties of the standard GNSPs by aligning them on Au electrodes using the dielectrophoresis techniques [54,55], as detailed in Fig. S7 (a)-(b). We found that the sheet resistance R of a single layer GNSPs to be ranging from ~7.0 kΩ/to ~7.8 kΩ/at room temperature, which were larger than that of typical pristine graphene sheet resistance (~1 kΩ/), but were significantly smaller than those values (~50 kΩ/to ~ 30 kΩ/) reported for lithographically patterned single-layer GNSPS of comparable widths (100 nm−1 μm) [56], suggesting good conducting properties of our GNSPS even in the absence of excess doping. If we take the work function of undoped graphene to be 4.50 eV [50], the electron density n_{2D} of our standard GNSPs with $\Phi = 4.45$ eV (and therefore a Fermi energy $E_F \sim 0.05$ eV above the Dirac point) is estimated to be $n_{2D} = (E_F/\hbar v_F)^2/\pi \sim 1.0 \times 10^{11}$ cm^{-2} for a Fermi velocity $v_F = 10^6$ m/s [3]. Therefore, the electrical mobility μ of our GNSPs is found to be$\mu = (n_{2D}\, e\, R_{\square})^{-1} = 8000$–$9000$ cm^2/V-s at room temperature, which is 5–10 times smaller than that of our typical PECVD-grown graphene sheets [42] and is about $10^2 \sim 10^3$ times better than that of the vertical graphene nano-sheets reported to date [40,41].

4. Discussion

Based on the aforementioned experimental results, we propose the following mechanism for the branching of GNSPs under excess 1,2-DCB. After initial vertical nucleation of a few honeycomb lattices on the copper substrate as illustrated in Fig. 1(a), the graphene edges may be chlorine terminated due to chlorine radicals dissociated from 1,2-DCB [57]. These chlorine terminated edges are chemically activated because of electron withdrawal from carbon atoms. Thus, electron-rich aromatic species (*e.g.*, 1,2-DCB and its derivatives) can be drawn to the electron deficient carbon atoms. Given that the zigzag edges of graphene are more likely to react with chlorine or 1,2-DCB molecules due to steric hindrance at the armchair edges, we first consider the growth mechanism along the zigzag edges. As depicted in Fig. 4-I, 1,2-DCB molecule may attach to the graphene zigzag edge via nucleophilic aromatic substitution and produce HCl (Fig. 4-II) by reaction with either nearby hydrogen atoms or hydrogen plasma to restore the sp^2 hybridization, as illustrated in Fig. 4-III. The production of HCl is consistent with our RGA data, and restoring sp^2 hybridization is energetically favorable. Conversely, the plasma processes may create radical-terminated graphene edges that react with radicals derived from 1,2-DCB. Furthermore, the 1,2-DCB molecule may react with hydrogen plasma and lose both chlorine atoms to become either benzene or C_6 radicals, which are highly reactive aromatics that could react with graphene edges. Based on our RGA data as exemplified in Fig. 1(b) and (c), all of these schemes may contribute the attachment of aromatic rings to GNSPs. However, given the highly complex nature of plasma chemistry [58], at this time we cannot identify which scheme is dominant.

From the illustration in Fig. 4-III it is also feasible to conjecture the formation of 5-membered rings along the zigzag edges during the growth of GNSPs. In general the formation of 5-membered rings (pentagons) would be accompanied by other defects such as 8-membered rings (octagons), which would lead to line defects that buckled into ridges and distorted the planar structures, as reported previously in scanning tunneling microscopic studies of graphene grown on Ni (111) substrate [59]. Such buckled planes could also contribute to larger interplanar spacing in the GNSPs. However, given that our TEM studies of the planar structures of GNSPs always revealed multiple sets of 6-fold Bragg diffraction spots with small angles relative to each other (see Fig. 3(d) and (h)), which are more consistent with turbostratic multilayers of predominantly 6-fold symmetric planar structures, we believe that the formation of defected structures along the zigzag edges of the GNSPs was unlikely a dominant growth mechanism.

The steps described from Fig. 4-I to III are repeated to yield the configuration shown in Fig. 4-IV. Finally, spatial gaps between edges with 1,2-DCB molecules attached can be filled in with carbon radicals dissociated from either methane or 1,2-DCB to complete the graphene lattice illustrated in Fig. 4-V. When excess 1,2-DCB is present, the graphene edges may become saturated with 1,2-DCB molecules, *i.e.*, 1,2-DCB molecules may attach to adjacent graphene edge sites as in Fig. 4-VI. Saturation of the graphene edges with 1,2-DCB molecules will necessarily result in strain and branching due to steric hindrance. (See Fig. S8 for the illustration of a 3D model). The sp^3 branching at the strained graphene sites may be achieved by the attachment of chlorine radicals (Fig. 4-VII), which is consistent with our EDS observation that chlorine is primarily present at the branching sites of nano-flowers grown under excess 1,2-DCB. On the other hand, when 1,2-DCB is relatively dilute, the graphene zigzag edges are more likely terminated by hydrogen, which could either react with the Cl atom in 1,2-DCB, release HCl while extending the length of graphene, or simply react with carbon radicals dissociated from either methane or 1,2-DCB to further the growth of graphene.

Thus far we have only described a growth mechanism along the zigzag edges of GNSPs. A similar mechanism may take place along the armchair edge, but at a slower rate due to steric hindrance of both edge chlorination (chemical activation) and 1,2-DCB attachment. Alternatively, 1,2-DCB molecules may selectively attach to zigzag edges while carbon radicals attach to both armchair and zigzag edges as has been proposed in the growth of vertically oriented graphene sheets [40,41]. Either case is consistent with the large aspect ratios of our GNSPs. Additionally, the prominent

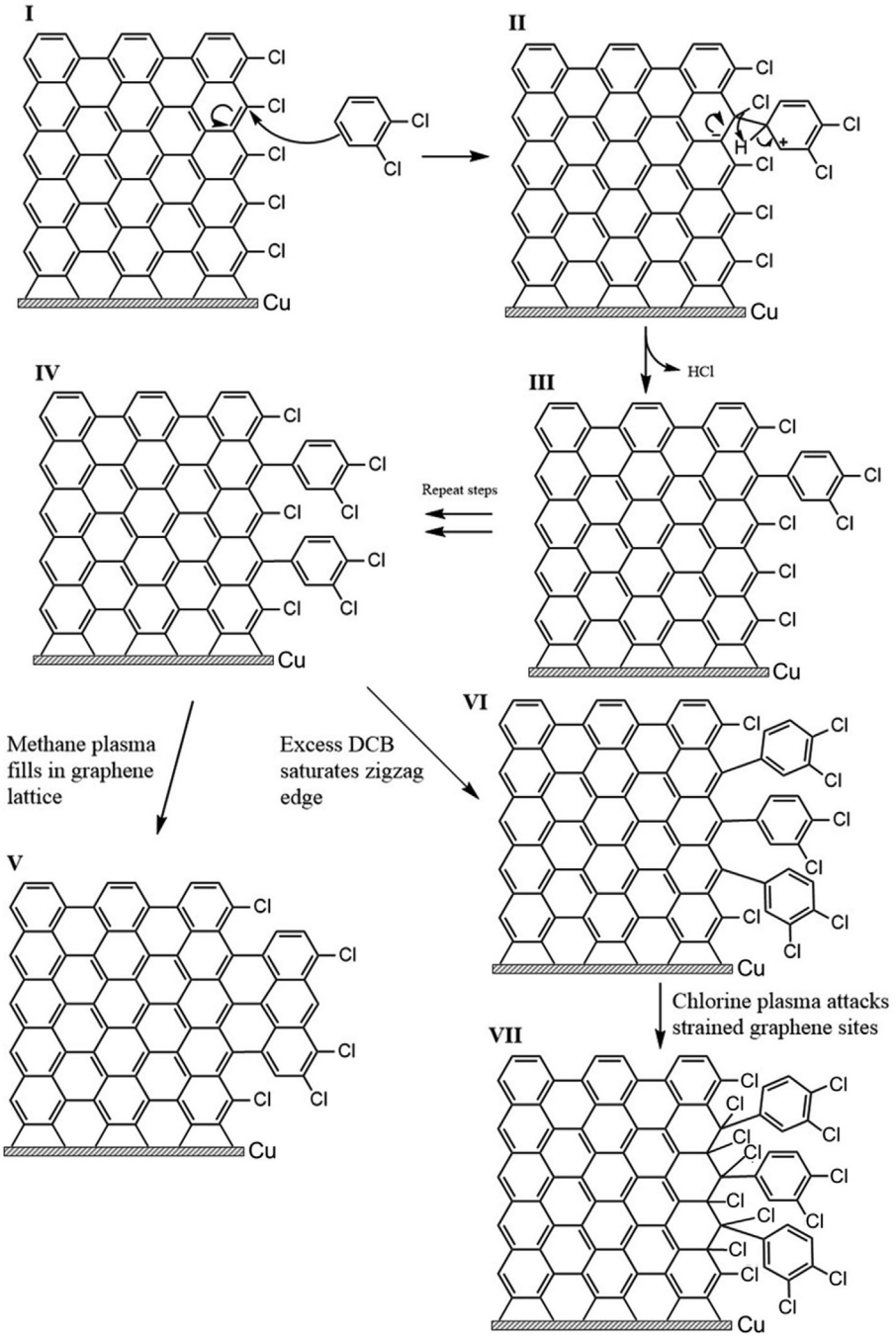

Fig. 4. Proposed mechanism of growth and branching of GNSPs with steps labeled as Roman numerals **I** ~ **VII**. Details of the mechanism are described in the text.

presence of C_6 radicals and C_6H_6 molecules in our plasma growth process is likely important for increasing the growth rate and yield of GNSPs because graphene structures can be more effectively assembled from these molecules than from C_2 radicals. This notion is further corroborated by recent studies using solution plasma-induced formation of nano-carbons [60], which revealed that among hexane, hexadecane, cyclohexane and benzene, the synthesis rate from benzene was the highest.

Despite overall consistency of the aforementioned model with our experimental findings, we note that a radical-based growth mechanism is also possible for the growth of the GNSPs. Further computational studies will be helpful to confirm or revise our conjectures, particularly if short-lived radicals that are difficult to detect empirically may play an important role in the growth mechanism. All in all, our empirical findings are suggestive of the importance of both 1,2-DCB precursor molecules and the resulting C_6, C_6H_6 and chlorine radicals in hydrogen plasma for mediating rapid vertical growth of GNSPs with large aspect ratios. In contrast to other reports for PECVD-grown vertical graphene sheets to date that generally required pretreatment of the substrates and additional substrate heating from 500 °C to 1000 °C [40,41], our single-step, low-power growth process requires neither active heating nor pretreatment of the substrates, indicating the effectiveness of 1,2-DCB as seeding molecules for the vertical growth of GNSPs.

5. Conclusions

In summary, we have developed a new high-yield single-step method for growing large quantity GNSPs on various transition-metal substrates by means of PECVD and aromatic precursors such as 1,2-DCB molecules. This efficient growth method does not require any active heating and can reproducibly produce a high yield of ~10 g/m^2 within 20 min at a relative low power of $\leq$60 W. Moreover, the GNSPs thus produced reveal large aspect ratios (up to >~130) and can be easily transferred from the growth substrate to any other substrates. Therefore, this new growth method is highly promising for mass production of GNSPs. From studies of the Raman spectra, SEM images, UPS, TEM images, EDS and electrical conductivity of these GNSPs as functions of the growth parameters, we have also confirmed the high-quality of these GNSPs and found the correlation of the properties of GNSPs with the growth parameters. Based on our experimental findings, we propose a growth and branching mechanism of GNSPs that suggests the important role of the 1,2-DCB precursor molecules in assisting the vertical growth and determining the morphology as well as the large aspect ratio of GNSPs. These findings therefore open up a new pathway to large-scale, inexpensive mass production of high-quality GNSPs for such large-scale applications as supercapacitors and photovoltaic cells.

Acknowledgment

This work at Caltech was supported by the Grubstake Award, and that at Rice University was sponsored by the Air Force Office of Scientific Research (FA9550-14-1-0111). The authors acknowledge the use of XPS/UPS at the Beckman Institute and the AFM and four-probe station at the Kavli Nanoscience Institute. W.–S. Tseng acknowledges the partial support from the Dragon Gate Program by the Ministry of Science and Technology in Taiwan. Yiran Zhang and Yiliang Li acknowledge financial support respectively from the Ziyuan College at the Shanghai Jiao Tong University in China and from the Tsien Excellence in Education Program (TEEP) at the Tsinghua University in China during their visit to Caltech as visiting undergraduate researchers.

Appendix A. Supplementary data

Supplementary data related to this article can be found at https://doi.org/10.1016/j.carbon.2017.12.058.

References

[1] A.K. Geim, K.S. Novoselov, The rise of graphene, Nat. Mater. 6 (2007) 183–191.
[2] A.K. Geim, Graphene: status and prospects, Science 324 (2009) 1530–1534.
[3] A.H. Castro Neto, F. Guinea, N.M.R. Peres, K.S. Novoselov, A.K. Geim, The electronic properties of graphene, Rev. Mod. Phys. 81 (2009) 109.
[4] K. Nakada, M. Fujita, G. Dresselhaus, M.S. Dresselhaus, Edge state in graphene ribbons: nanometer size effect and edge shape dependence, Phys. Rev. B 54 (1996) 17954–17961.
[5] K. Wakabayashi, M. Fujita, H. Ajiki, M. Sigrist, Electronic and magnetic properties of nanographite ribbons, Phys. Rev. B 59 (1999) 8271–8282.
[6] M.Y. Han, B. Ozyilmaz, Y. Zhang, P. Kim, Energy band-gap engineering of graphene nanoribbons, Phys. Rev. Lett. 98 (2007) 206805.
[7] A. Kimouche, M.M. Ervasti, R. Drost, S. Halonen, A. Harju, P.M. Joensuu, et al., Ultra-narrow metallic armchair graphene nanoribbons, Nature Commun 6 (2015) 10177.
[8] P. Ruffieux, S. Wang, B. Yang, C. Sánchez-Sánchez, J. Liu, T. Dienel, et al., On-surface synthesis of graphene nanoribbons with zigzag edge topology, Nature 531 (2016) 489–493.
[9] R. Faccio, P.A. Denis, H. Pardo, C. Goyenola, Á.W. Mombrú, Mechanical properties of graphene nanoribbons, J. Phys. Condens. Matter 21 (2009) 285304.
[10] C. Xiang, P.J. Cox, A. Kukovecz, B. Genorio, D.P. Hashim, Z. Yan, et al., Functionalized low defect graphene nanoribbons and polyurethane composite film for improved gas barrier and mechanical performances, ACS Nano 7 (2013) 10380–10386.
[11] A. Behnam, A.S. Lyons, M.H. Bae, E.K. Chow, S. Islam, C.M. Neumann, et al., Transport in nanoribbon interconnects obtained from graphene grown by chemical vapor deposition, Nano Lett. 12 (2012) 4424–4430.
[12] W.S. Hwang, P. Zhao, K. Tahy, L.O. Nyakiti, V.D. Wheeler, R.L. Myers-Ward, et al., Graphene nanoribbon field-effect transistors on wafer-scale epitaxial graphene on SiC substrates, APL Mat 3 (2015), 011101.
[13] X. Li, X. Wang, L. Zhang, S. Lee, H. Dai, Chemically derived, ultrasmooth graphene nanoribbon semiconductors, Science 319 (2008) 1229–1232.
[14] Q. Wang, R. Kitaura, S. Suzuki, Y. Miyauchi, K. Matsuda, Y. Yamamoto, et al., Fabrication and in situ transmission electron microscope characterization of free-standing graphene nanoribbon devices, ACS Nano 10 (2016) 1475–1480.
[15] Q.H. Wang, Z. Jin, K.K. Kim, A.J. Hilmer, G.L.C. Paulus, C.-J. Shih, M.-H. Ham, J.D. Sanchez-Yamagishi, K. Watanabe, T. Taniguchi, J. Kong, P. Jarillo-Herrero, M.S. Strano, Understanding and controlling the substrate effect on graphene electron-transfer chemistry via reactivity imprint lithography, Nature Chem. 4 (2012) 724–732.
[16] W. Han, R.K. Kawakami, M. Gmitra, J. Fabian, Graphene spintronics, Nat. Nanotechnol. 9 (2014) 794–807.
[17] G.Z. Magda, X. Jin, I. Hagymási, P. Vancsó, Z. Osváth, P. Nemes-Incze, et al., Room-temperature magnetic order on zigzag edges of narrow graphene nanoribbons, Nature 514 (2014) 608–611.
[18] A.N. Grigorenko, M. Polini, K.S. Novoselov, Graphene plasmonics, Nat. Photon. 6 (2012) 749–758.
[19] V.W. Brar, M.S. Jang, M. Sherrott, J.J. Lopez, H.A. Atwater, Highly confined tunable mid-infrared plasmonics in graphene Nanoresonators, Nano Lett. 13 (2013) 2541–2547.
[20] V.W. Brar, M.S. Jang, M. Sherrott, S. Kim, J.J. Lopez, L.B. Kim, et al., Hybrid surface-phonon-plasmon polariton modes in graphene/monolayer h-BN heterostructures, Nano Lett. 14 (2014) 3876–3880.
[21] S. Myung, A. Solanki, C. Kim, J. Park, K.S. Kim, K.B. Lee, Graphene-encapsulated nanoparticle-based biosensor for the selective detection of cancer biomarkers, Adv. Mater. 23 (2011) 2221.
[22] Z. Jin, W. Sun, Y. Ke, C.-J. Shih, G.L.C. Paulus, Q.H. Wang, B. Mu, P. Yin, M.S. Strano, Metallized DNA nanolithography for encoding and transferring spatial information for graphene patterning, Nature Comm. 4 (2013) 1663.
[23] P. Ahuja, R.K. Sharma, G. Singh, Solid-state, high-performance supercapacitor using graphene nanoribbons embedded with zinc manganite, J. Mater. Chem. 3 (2015) 4931–4937.
[24] T.J. Echtermeyer, L. Britnell, P.K. Jasnos, A. Lombardo, R.V. Gorbachev, A.N. Grigorenko, et al., Strong plasmonic enhancement of photovoltage in graphene, Nature Commun 2 (2011) 458.
[25] X. Wang, H. Dai, Etching and narrowing of graphene from the edges, Nature Chem. 2 (2010) 661–665.
[26] V. Abramova, A. Slesarev, J.M. Tour, Meniscus-mask lithography for narrow graphene nanoribbons, ACS Nano 7 (2013) 6894–6898.
[27] J. Cai, P. Ruffieux, R. Jaafar, M. Bieri, T. Braun, S. Bankenburg, et al., Atomically precise bottom-up fabrication of graphene nanoribbons, Nature 466 (2010) 470–473.
[28] T.H. Vo, M. Shekhirev, D.A. Kunkel, M.D. Morton, E. Berglund, L. Kong, et al., A. Large-scale solution synthesis of narrow graphene nanoribbons, Nature Commun 5 (2014) 3189.
[29] C. Long, Y. Hernandez, X. Feng, K. Müllen, From nanographene and graphene nanoribbons to sheets: chemical synthesis, Angew. Chem. Int. Ed. 51 (2012) 7640–7654.
[30] A. Narita, I.A. Verzhbitskiy, W. Frederickx, K.S. Mali, S.A. Jensen, M.R. Hansen, et al., Bottom-up synthesis of liquid-phase-processable graphene nanoribbons with near-infrared absorption, ACS Nano 8 (2014) 11622–11630.
[31] M. Daigle, D. Miao, A. Lucotti, M. Tommasini, J.-F. Morin, Helically coiled graphene nanoribbons, Angew. Chem. Int. Ed. 56 (2017) 6213.
[32] W. Yang, A. Lucotti, M. Tommasini, W.A. Chalifoux, Bottom-up synthesis of soluble and narrow graphene nanoribbons using alkyne benzannulations, Am. Chem. Soc. 138 (2016) 9137.
[33] M.B. Goldfinger, T.M. Swager, Fused polycyclic aromatics via electrophile-induced cyclization reactions: application to the synthesis of graphite ribbons, J. Am. Chem. Soc. 116 (1994) 7895.
[34] R.S. Jordan, Y. Wang, R.D. McCurdy, M.T. Yeung, S.I. Khan, R.B. Kaner, et al., Synthesis of graphene nanoribbons via the topochemical polymerization and subsequent aromatization of a diacetylene precursor, Chem. 1 (2016) 78.
[35] T.J. Sisto, Y. Zhong, B. Zhang, M.T. Trinh, K. Miyata, X. Zhong, Long, atomically precise Donor–Acceptor cove-edge nanoribbons as electron acceptors, J. Am. Chem. Soc. 139 (2017) 5648.
[36] B. Genorio, W. Lu, A.M. Dimiev, Y. Zhu, A.-R.O. Raji, B. Novosel, et al., In situ intercalation replacement and selective functionalization of graphene nanoribbon stacks, ACS Nano 6 (2012) 4231–4240.
[37] D.V. Kosynkin, W. Lu, A. Sinitskii, G. Pera, Z. Sun, J.M. Tour, Highly conductive graphene nanoribbons by longitudinal splitting of carbon nanotubes by potassium vapor, ACS Nano 5 (2011) 968–974.
[38] C.H.A. Wong, C.K. Chua, B. Khezri, R.D. Webster, M. Pumera, Graphene oxide nanoribbons from the oxidative opening of carbon nanotubes retain electrochemically active metallic impurities, Angew. Chem. Int. Ed. 52 (2013) 8685–8688.
[39] A. Ambrosi, C.K. Chua, N.M. Latiff, A.H. Loo, C.H.A. Wong, A.Y.S. Eng, A. Bonanni, M. Pumera, Graphene and its electrochemistry – an update, Chem. Soc. Rev. 45 (2016) 2458–2493.
[40] Z. Bo, Y. Yang, J. Chen, K. Yu, J. Yan, K. Cen, Plasma-enhanced chemical vapor

deposition synthesis of vertically oriented graphene nanosheets, Nanoscale 5 (2013) 5180–5204 references therein).
[41] M. Hiramatsu, M. Hori, Carbon Nanowalls: Synthesis and Emerging Applications, ISBN 978-3-211-99718-5, Springer, 2010. and references therein).
[42] D.A. Boyd, W.H. Lin, C.C. Hsu, M.L. Teague, C.C. Chen, Y.Y. Lo, et al., Single-step deposition of high-mobility graphene at reduced temperatures, Nat. Commun. 6 (2015) 6620.
[43] A.C. Ferrari, J.C. Meyer, V. Scardaci, C. Casiraghi, M. Lazzeri, F. Mauri, et al., Raman spectrum of graphene and graphene layers, Phys. Rev. Lett. 97 (2006), 187401.
[44] A.C. Ferrari, Raman spectroscopy of graphene and graphite: disorder, electron-phonon coupling, doping and non-adiabatic effects, Solid State Commun. 143 (2007) 47–57.
[45] A.M. Dimiev, G. Ceriotti, N. Behabtu, D. Zakhidov, M. Pasquali, R. Saito, et al., Direct real-time monitoring of stage transitions in graphite intercalation compounds, ACS Nano 7 (2013) 2773–2780.
[46] A.M. Dimiev, S.M. Bachilo, R. Saito, J.M. Tour, Reversible formation of ammonium persulfate/sulfuric acid graphite intercalation compounds and their peculiar Raman spectra, ACS Nano 6 (2012) 7842–7849.
[47] Z. Sun, A.-R.O. Raji, Y. Zhu, C. Xiang, Z. Yan, C. Kittrell, et al., Large-area Bernal-stacked bi-, tri-, and tetra-layer graphene, ACS Nano 6 (2012) 9790–9796.
[48] Z.K. Liu, J.H. Li, Z.H. Sun, G.A. Tai, S.P. Lau, F. Yan, The application of highly doped single-layer graphene as the top electrodes of semitransparent organic solar cells, ACS Nano 6 (2012) 810–818.
[49] C.L. Hsu, C.T. Lin, J.H. Huang, C.W. Chu, K.H. Wei, L.J. Li, Layer-by-layer graphene/TCNQ stacked films as conducting anodes for organic solar cells, ACS Nano 6 (2012) 5031–5039.
[50] H. Kim, S.H. Bae, T.H. Han, K.G. Lim, J.H. Ahn, T.W. Lee, Organic solar cells using CVD-grown graphene electrodes, Nanotechnology 25 (2014), 014012.
[51] Y. Zhou, D.S. Fox, P. Maguire, R. O'Connell, R. Masters, C. Rodenburg, et al., Quantitative secondary electron imaging for work function extraction at atomic level and layer identification of graphene, Sci. Rep. 6 (2016), 21045.
[52] L.G. Cancado, K. Takai, T. Enoki, M. Endo, Y.A. Kim, H. Mizusaki, et al., General equation for the determination of the crystallite size La of nanographite by Raman spectroscopy, Appl. Phys. Lett. 88 (2006), 163106.
[53] L.M. Malard, M.A. Pimenta, G. Dresselhaus, M.S. Dresselhaus, Raman spectroscopy in graphene, Phys. Rep. 473 (2009) 51–87.
[54] R. Krupke, F. Hennrich, H.V. Löhneysen, M.M. Kappes, Separation of metallic from semiconducting single-walled carbon nanotubes, Science 301 (2003) 344–347.
[55] A. Vijayaraghavan, C. Sciascia, S. Dehm, A. Lombardo, A. Bonetti, A.C. Ferrari, et al., Dielectrophoretic assembly of high-density arrays of individual graphene devices for rapid screening, ACS Nano 3 (2009) 1729–1734.
[56] Z.J. Qi, J.A. Rodríguez-Manzo, A.R. Botello-Mendez, S.J. Hong, E.A. Stach, Y.W. Park, et al., Correlating atomic structure and transport in suspended graphene nanoribbons, Nano Lett. 14 (2014) 4238–4244.
[57] J. We, L. Xie, Y. Li, H. Wang, Y. Ouyang, J. Guo, et al., Controlled chlorine plasma reaction for noninvasive graphene doping, J. Am. Chem. Soc. 133 (2011) 19668–19671.
[58] D. Herrebout, M. Bogaerts, M. Yan, R. Gijbels, W. Goedheer, E. Dekempeneer, One-dimensional fluid model for an rf methane plasma of interest in deposition of diamond-like carbon layers, J. Appl. Phys. 90 (2001) 570–579.
[59] J. Lahiri, Y. Lin, P. Bozkurt, I.I. Oleynik, M. Batzill, An extended defect in graphene as a metallic wire, Nat. Nanotechnol. 5 (2010) 326–329.
[60] T. Morishita, T. Ueno, G. Panomsuwan, J. Hieda, A. Yoshida, M.A. Bratescu, et al., Fastest formation routes of nanocarbons in solution plasma processes, Sci. Rep. 6 (2016), 36880.